SPLEEN

PIV MEASUREMENTS

Technical Summary of the instrumentation, measurement techniques and data reduction for the Particle Image Velocimetry (PIV) measurements performed on the test case SPLEEN C1

SPLEEN Identifier	SPLEEN-HSTC-DB-MeasurementTechniques_PIV_v2
Author(s) and affiliation	S. Lavagnoli, G. Lopes, S. Simonassi, F.A.M. Torre, M. Okada (VKI)
Comments	Technical report that describes the instrumentation, measurement techniques, measurement locations, data processing and uncertainty of **PIV measurements** performed on the SPLEEN C1 test case in the high-speed linear cascade S1/C of the von Karman Institute.

DOCUMENT HISTORY			
Version	**Date**	**Changed by**	**Reason of change**
PIV_v1	01.12.2023	M. Okada, S. Lavagnoli	Description of PIV measurements.
PIV_v2	04.12.2023	M. Okada	Notes and figure added in 2.2.2.4 to enhance description of the setup.

Contents

List of Figures

List of Tables

List of Symbols

A	cross-section area [m^2]	M	Mach number [-]
a	Sound speed [m s^{-1}]	P	pressure [Pa]
B2B	Blade-to(2)-Blade	q	dynamic pressure [Pa]
C	Blade chord [m]	PMFR	Purge mass flow rate [% of main flow]
C_D	Drag coefficient [-]	R	Specific gas constant [J kg^{-1} K^{-1}]
COP	Cascade Outlet Plane	Re	Reynolds number [-]
DEHS	Di-Ethyl-Hexyl-Sebacat	T	Temperature [K]
FOV	Field Of View	TE	Trailing edge
g	Cascade passage pitch [m]	TI	Turbulence intensity [%]
H	Cascade span [m]	V	Mean velocity [m/s]
LE	Leading edge	WG	Wake Generator
LPT	Low-pressure turbine	Y	Pressure drop coefficient [-]
l	Length [m]	2D2C	Two-dimensional two-component
$\dot{m}$	mass flow rate [kg s^{-1}]	2D3C	Two-dimensional three-component

Greek Symbols

α	absolute incidence angle [deg]
β	grid porosity [-] Primary flow direction (yaw angle) [deg]
γ	heat capacity ratio [-] Flow pitch angle [deg]
ϕ	diameter [mm]
Φ	flow coefficient [-]
μ	dynamic viscosity [kg m^{-1} s^{-1}]
ρ	density [kg m^{-3}]
σ	Standard deviation

Subscripts

0	total conditions axis origin	r	rods
amb	Ambient	rad	radial
ax / axi	Axial	s	static conditions
bar	WG bar	tan / tang	tangential
BS	bar support	TG	turbulence grid
c	true chord	is	isentropic
in	inlet conditions (of the num. domain or cascade)	WG	wake generator
main	main flow	x	x-direction
out	cascade outlet	y	y-direction
purge	purge flow	z	z-direction

1 Introduction

The present report contains information on the experimental setup and hardware concerning PIV measurements performed on the cascade SPLEEN C1 (Chapter 2). Chapter 3 provides definitions for quantities reported in the database (losses, angles, etc.) and exposes the data reduction techniques applied to the PIV image acquisitions. Lastly, Chapter 4 reports the uncertainty analysis of the measured and derived quantities from the PIV images.

This document specifically focuses on the PIV measurements performed on the SPLEEN C1 high-speed low-pressure turbine cascade. For a complete description of the experimental setup, instrumentation, measurement uncertainties, geometries used in the open-access SPLEEN test case refer to the open-access database that can be found at https://zenodo.org/doi/10.5281/zenodo.7264761

2 Experimental setup

The aim of this section is to present the linear cascade experimental setup for the PIV measurements of the SPLEEN C1 turbine cascade. This section defines the cascade reference system used for PIV measurements and the measurement chain.

2.1 The high-speed turbine cascade facility

The linear cascade measurements are conducted in the high-speed, low Reynolds facility S-1/C of the von Karman Institute. A sketch describing the facility is shown in Figure 2-1 This wind tunnel is a continuous closed-loop facility driven by a 615 kW 13 stages axial flow compressor. A heat exchanger allows controlling the flow temperature at near atmospheric condition. The mass flow is regulated via the adjustment of the compressor rotational speed and via a pressure regulation valve. A vacuum pump allows lowering the tunnel absolute pressure to below 8,000 Pascal. The cascade test section is in the first elbow of the wind tunnel loop (upper left elbow in Figure 2-1) following the diffuser. The cylindrical rear part of the diffuser is functioning as a settling chamber for the cascade test section. Wire meshes and honeycombs upstream of the test section ensure homogeneous flow conditions.

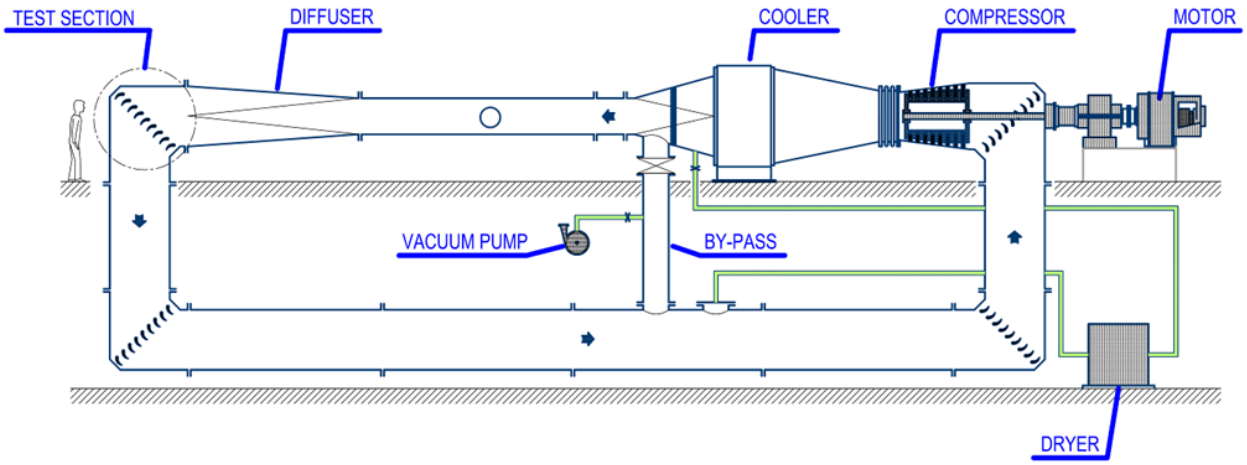

Figure 2-1: S-1/C wind tunnel.

A sketch and a picture of a typical LPT cascade model are shown in Figure 2-2. A bell mouth as well as vertical and lateral contractions provide the transition between the original circular parts of the wind tunnel and the cascade. The linear cascade ensemble is made up of several full blades (depending on the required pitch and chord length) plus two end-blocks at the cascade extremities. The cascade is mounted in between two large circular rotating sidewalls, which allow the fine adaptation of the inlet flow angle. Turbulence grids can be placed upstream the test section to increase the free-stream turbulence intensity.

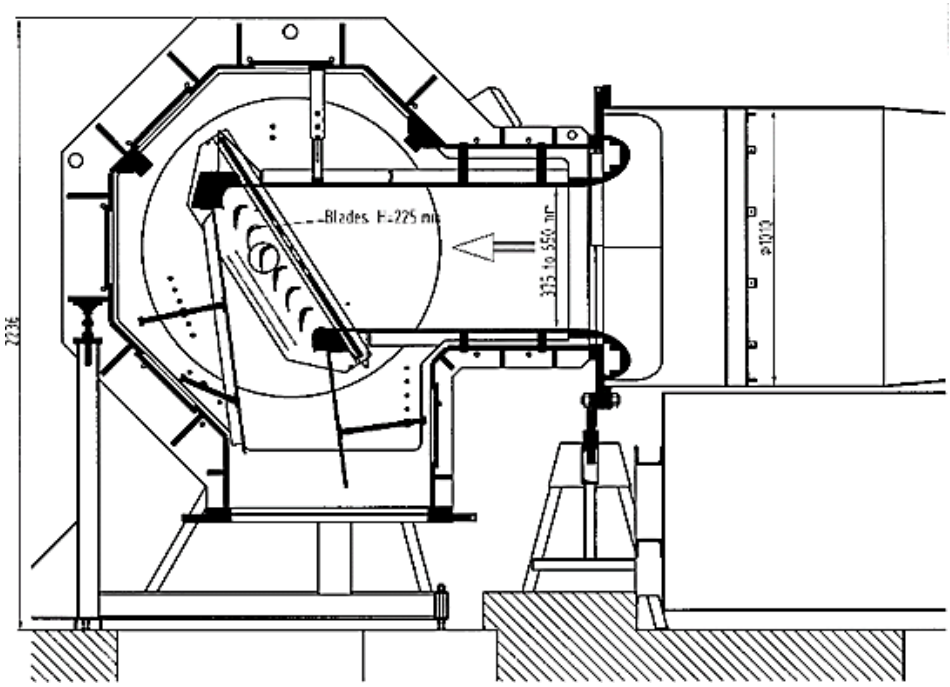

Figure 2-2: Sketch of typical S-1/C turbomachinery test section.

2.2 Instrumentation

2.2.1 Measurement planes

The cartesian reference system used is presented in Figure 2-3. The origin point of the reference system sits at the intersection of the central blade LE with the cavity bottom endwall (this is the endwall at the side of the boundary layer lip and wake generator). The spanwise coordinate, z, increases from the origin towards the blade midspan. The pitchwise coordinate, y, increases towards the pressure side of the central blade to the suction side of the closest blade and the axial chordwise coordinate, x, increases from the origin towards the TE following a direction perpendicular to the plane containing the LE of all blades.

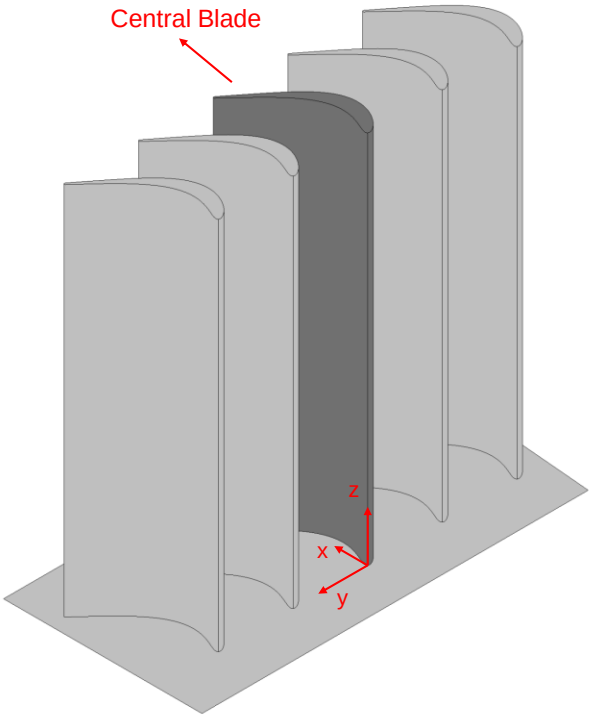

Figure 2-3: Measurement reference system.

Figure 2-4 illustrates the locations of the measurement planes across the cascade. Seven planes are selected at relevant axial stations:

- Plane ref. corresponds to the measurement plane of the reference total pressure and total temperature. The location of this plane depends on the rotation of the whole cascade. It sits at least 1 m upstream of the central blade LE.
- Plane 01 is aligned with the plane of rotation of the wake generator and it is located at $x = -1.12C_{ax}$.
- Plane 02 corresponds to the approximate exit location of the cavity slot. It is located at $x = -0.50C_{ax}$.
- Plane 03 is located at $x = 0C_{ax}$ (Plane containing LE of all blades).
- Plane 04 is located at $x = C_{ax}$ (Plane containing TE of all blades).
- Plane 05 and Plane 06 are parallel to Plane 04. Used to characterize the outlet flow field. Plane 05 and 06 are located at $x = 1.25C_{ax}$ and $x = 1.50C_{ax}$, respectively.

The location of the measurement planes as function of the blade axial chord is given in Table 2-1.

Table 2-1: Distance between measurement planes

Upstream of LE		Blade		Downstream of TE	
Plane 01	**Plane 02**	**Plane 03**	**Plane 04**	**Plane 05**	**Plane 06**
$-1.12C_{ax}$	$-0.50C_{ax}$	$0.00C_{ax}$	$1.00C_{ax}$	$1.25C_{ax}$	$1.50C_{ax}$

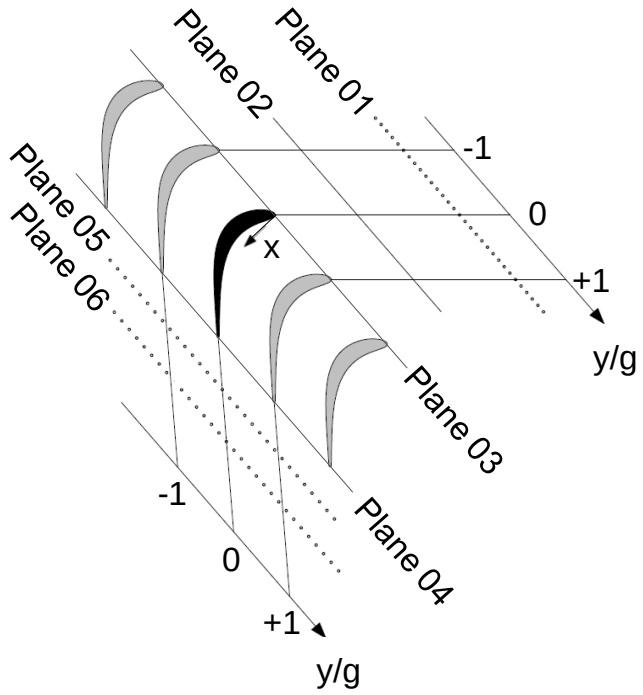

Figure 2-4: Location of measurement planes. Plane ref. not included.

2.2.2 PIV measurements

2.2.2.1 Test configuration

The cascade configuration for PIV measurements is presented in Table 2-2. The measurements were performed solely on the SPLEEN C1 cascade equipped with a injection cavity installed in the bottom endwall (cavity **Aref**), operated **without** purge flow injection. The effect of freestream turbulence was investigated by installing and removing the upstream turbulence grid. The wake generator was **not** installed during the PIV test campaign.

Table 2-2: SPLEEN C1 cascade configuration for PIV measurements.

Endwall cavity	Aref
Purge flow rate	0.0% (No purge flow)
Turbulence grid	With / Without
Wake generator	Without

Figure 2-5 illustrates the field of view (FOV) of the three PIV configurations carried out for the SPLEEN C1 cascade. The first configuration aims measurements on the midspan blade-to-blade (B2B) plane at the cascade inlet plane using a stereoscopic two-dimensional three-component (2D3C) PIV setup. The second configuration measures at the midspan B2B plane in the cascade passage including a part of the cascade outlet using planar two-dimensional two-component (2D2C) PIV with a side-by-side camera setup. A third PIV configuration is used to measure on the cascade outlet plane (COP) near the endwall using a stereoscopic 2D3C PIV setup. The COP is located 0.5 C_{ax} downstream of the blade trailing edge plane where aerodynamic probe measurements were also acquired in previous test campaigns.

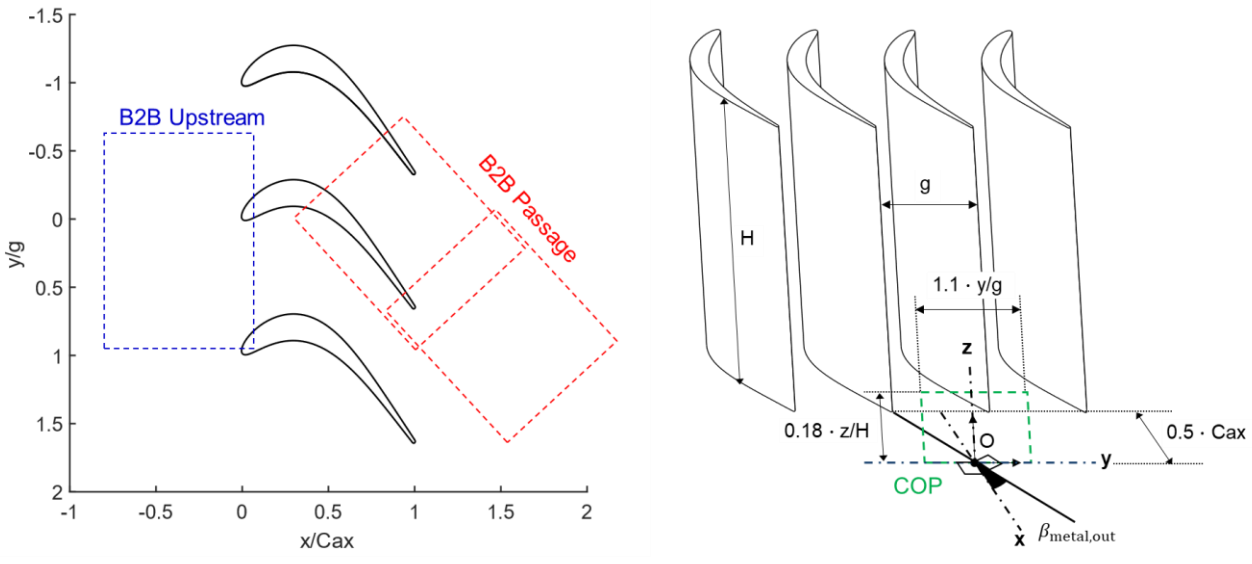

(A) Blade-to-blade plane (B) Cascade outlet plane

Figure 2-5: Field of view of the PIV measurements.

The PIV measurements for three test configurations were performed separately. The flow conditions investigated in the scope of this work are summarized in Table 2-3.

Table 2-3: Flow conditions of PIV measurements.

Turbulence grid	$Re_{out,is}$	$M_{out,is}$	B2B Upstream	B2B Passage	COP
With	70K	0.70	-	✓	✓
		0.90	✓	✓	✓
		0.95	-	✓	✓
	120K	0.70	✓	✓	-
		0.90	✓	✓	-
Without	70K	0.70	✓	✓	-
		0.90	✓	✓	-
		0.95	-	✓	-
	120K	0.70	✓	✓	-
		0.90	✓	✓	-

2.2.2.2 *Optical access*

The optical access for PIV measurements was realized by combining a cascade endwall window, side wall windows, and laser endoscopes. The orientation of the optical windows is presented in Figure 2-6. The endwall window is mounted on the cascade endwall aligned to the central blade providing a view in the spanwise direction. The two sidewall windows are attached to the sidewall of the elbow allowing access from the downstream of the cascade at different angles. The COP is parallel to the second row of pressure taps located 0.5 C_{ax} downstream of the blades trailing edge plane, and its center is aligned to the 16th pressure tap whose position coincides with the blade outlet metal angle line extension.

A new custom-made cascade endwall plate was designed and manufactured for optical measurements. The design of the optical cascade endwall is illustrated in Figure 2-7. The endwall plate features multiple pockets. The central pocket is used to mount the endwall window while the additional endwall pockets are mainly used for the installation of the image calibration system. These pockets are necessary to insert, manipulate, and extract the calibration plate system without touching the other optical system such as the endwall window and the cameras after having recorded the calibration images. These pockets are filled by metallic caps during the tests, flush-mounted to the internal test section wet surface. Some holes were added to one of the caps to provide access for a laser endoscope. The laser endoscope enable PIV measurements at the cascade inlet. Figure 2-8 and Figure 2-9 show the endwall and sidewall windows installed in the test section.

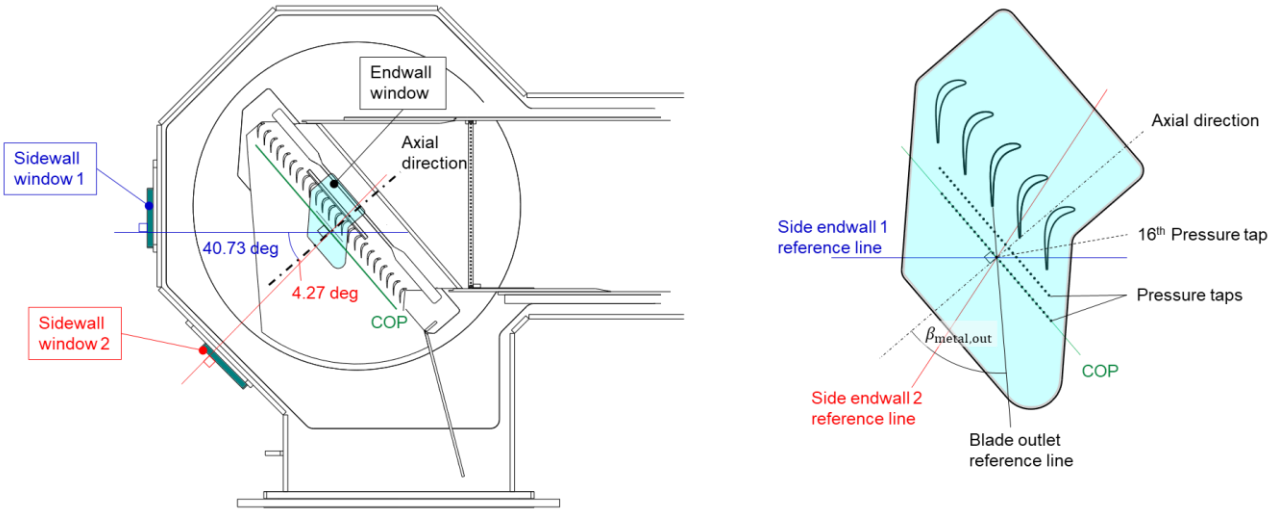

Figure 2-6 The orientation of optical windows of the test section.

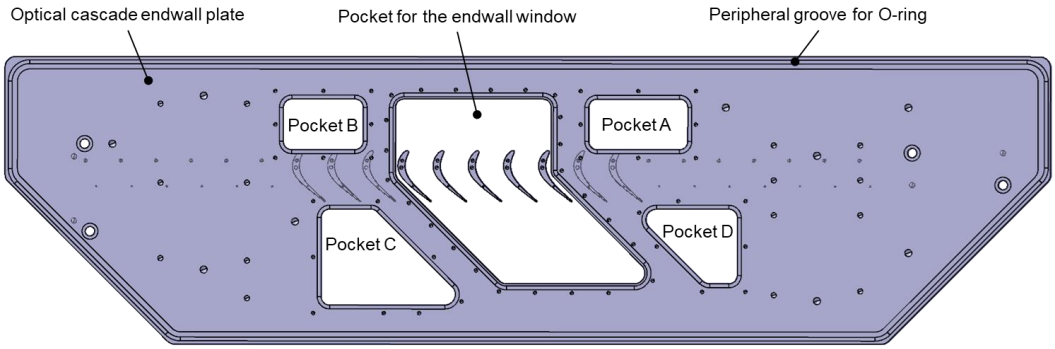

Figure 2-7 Design of optical endwall.

Figure 2-8 Endwall window.

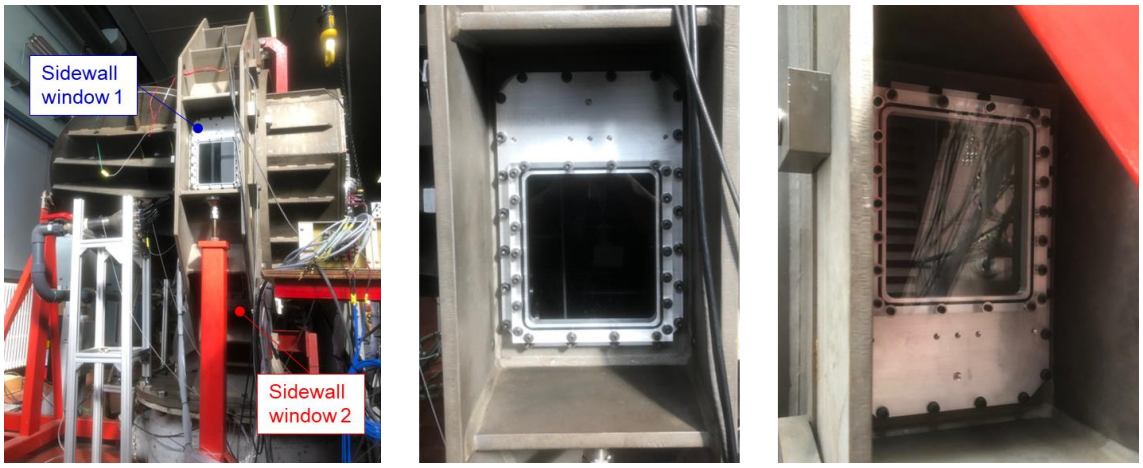

Figure 2-9 Sidewall windows.

For measurements with the B2B upstream configuration, pocket *A* located next to the endwall window was instrumented with the laser endoscope. Figure 2-10 illustrates the pocket cover *A* with three slots for the laser endoscopes. Dummy probes are used to close the unused plate holes.

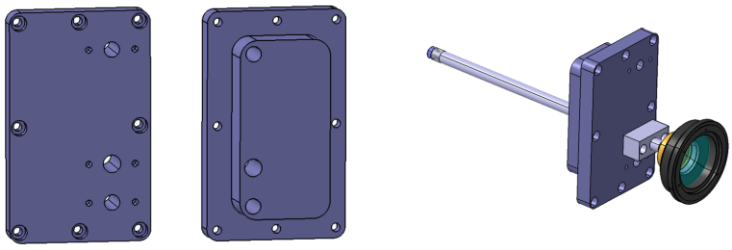

Figure 2-10 Endoscope access through Pocket cover A. (a) The design of pocket cover A. (b) The endoscope installed in the cover.

2.2.2.3 The B2B upstream inlet plane setup

Figure 2-11 and Figure 2-12 show schematics and photos of the PIV setup for the B2B upstream PIV configuration. The laser head was placed in front of the endwall of the test section. The laser beam emitted from the laser head was guided through a right-angle prism and mirror to the laser endoscope installed in pocket cover A. The laser endoscope delivers the laser beam inside the enclosed test section. The light sheet optics embedded in the tip of the endoscope forms the laser sheet. The laser sheet was placed at blade midspan. The yaw angle of the endoscope was aligned so that the central part of the laser sheet can illuminate the area between 0 and 60% of the blade axial chord upstream of the central blade LE. To minimize the light reflection, a matte-black paint was applied to the central 8 blades and endwall surface. The painted blade is shown in Figure 2-13.

Two cameras were placed in front of the endwall window to gain stereoscopic vision. Both cameras were equipped with a *Nikon AF Micro NIKKOR 60 mm f/2.8D* lens. The camera body was tilted with respect to the lens to satisfy the Scheimpflug condition using an adapter from *LaVision*. While the optimum angle between two cameras for stereoscopic vision is around 90 degrees, the limited space due to packed hardware such as the laser endoscope and the calibration traverse system imposed the maximum angle between the two cameras to be around 45 degrees. Note that the traverse system seen in Figure 2-12 is removed and the pocket hole is closed with a cover during the PIV flow measurements.

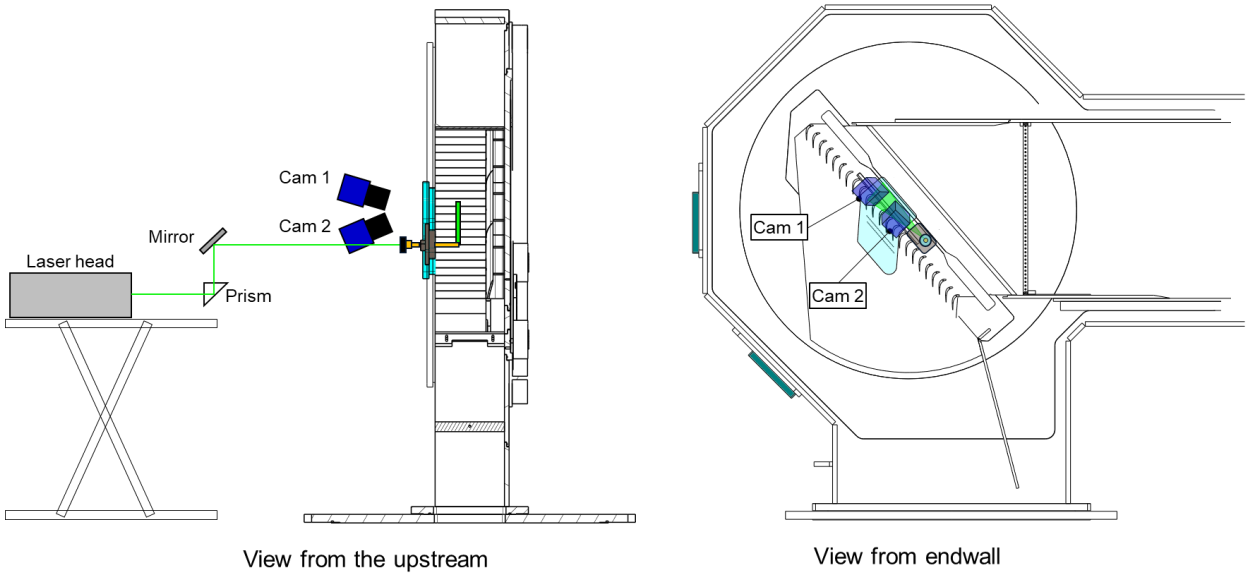

Figure 2-11 Schematics of the laser and camera setup for B2B upstream configuration.

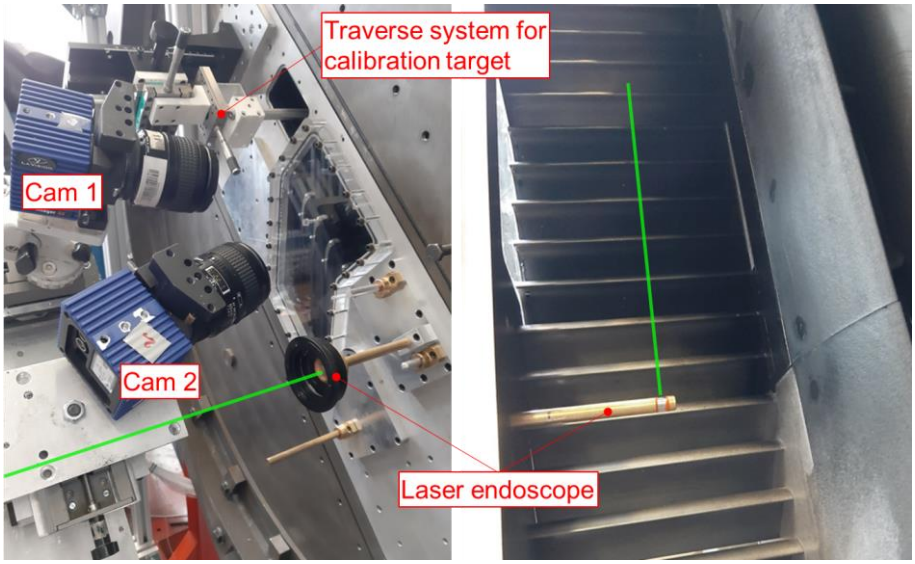

Figure 2-12 PIV setup for B2B upstream configuration.

Figure 2-13 Matte-black painted blade.

2.2.2.4 B2B passage setup

Figure 2-14 and Figure 2-15 show the schematics and photos of the PIV setup for the B2B upstream PIV configuration. The laser head was placed behind the sidewall of the test section. The laser beam emitted from the laser head was guided to the light sheet optics by two mirrors. The light sheet optics consists of the telescope lenses from *LaVision Divergent sheet optics* and a plano-concave cylindrical lens from *Thorlabs*. The light sheet was inserted into the test section through the sidewall window 2 so that a maximum area in the blade passage of the central blade (suction side) was illuminated. The position of the laser sheet was preliminary aligned before the camera setup, and the final alignment was done with the image calibration plate placed on the measurement plane.

A matte-black paint was applied to the endwall wall to minimize the reflection except for the area where the endwall pressure taps are located. Moreover, the central blade was coated with an orange-fluorescent paint to further reduce the light reflection. Fluorescent paint absorbs the laser light and emits fluorescent light at a longer wavelength. The thickness of the paint on the blade measured with feeler gauges was about 0.1 mm.

Two cameras were placed side by side facing the measurement plane through the endwall window to acquire two simultaneous FOVs as illustrated in Figure 2-5. While camera 1 focuses on the blade passage, camera 2 observes the cascade outlet plane. The FOVs of the two cameras were set to overlap by approximately 20%. Due to the relatively small FOV against the size of the cameras and lenses, camera 2 had to be slightly tilted to maintain the FOV overlap. Both cameras were equipped with a *Nikon AF Micro NIKKOR 60 mm f/2.8D* lens. While a Scheimpflug adaptor was mounted on each camera, no significant Scheimpflug angle was set since the image planes were nearly parallel to the measurement plane. The optical setup resulted in a scaling factor of about 48 pixels/mm. Furthermore, camera 1 was equipped with a 532 ± 10 nm band-pass filter.

Note 1: The lower part of the image captured with camera 2 for the B2B passage measurement was not satisfactorily illuminated due to optical access constraints (See Figure 2-16). Therefore, the velocity information in this region is expected to have 1.5-2.0 times higher uncertainty than in the other regions.

Note 2: The image quality of camera 2 for the B2B passage measurements without TG was not satisfactory due to a hardware setup issue. Nevertheless, the velocity fields were computed and included in the database to complement the description of the flow.

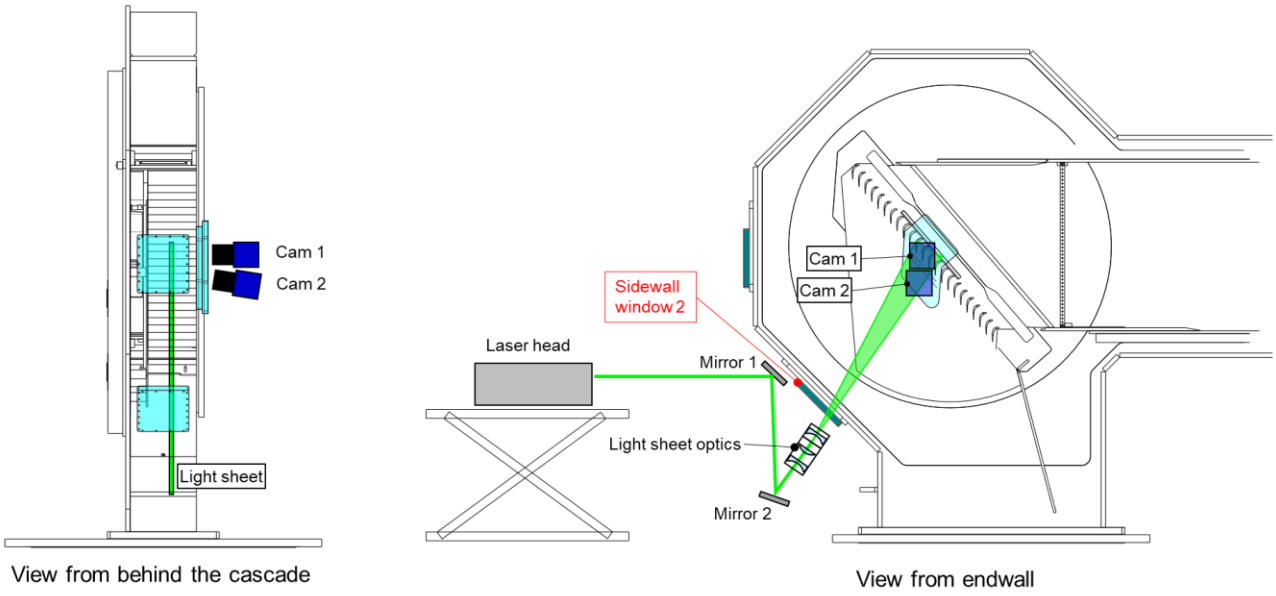

Figure 2-14 Schematics of the laser and camera setup for B2B passage configuration.

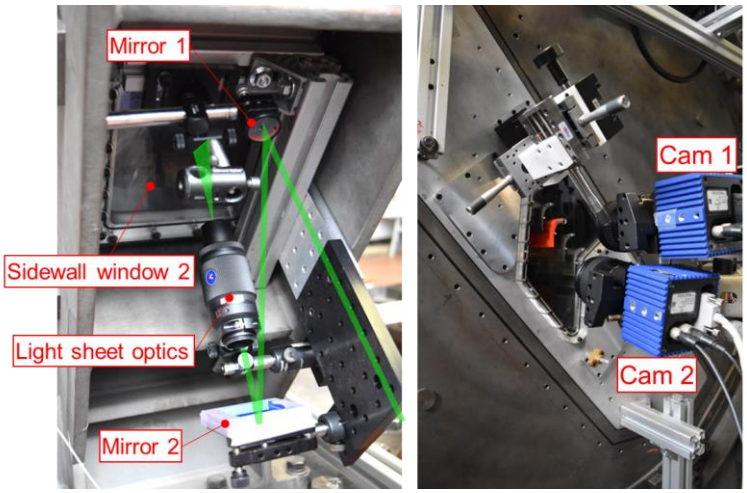

Figure 2-15 PIV setup for B2B Passage configuration.

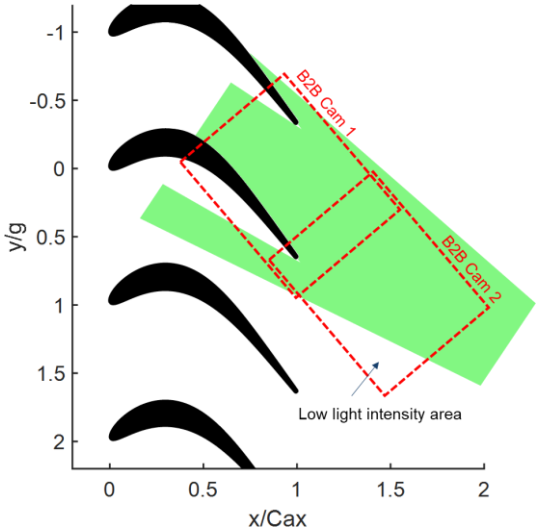

Figure 2-16 FOV and light sheet of the B2B passage PIV measurements.

2.2.2.5 COP setup

Figure 2-17 and Figure 2-18 show schematics and photos of the PIV setup for the COP PIV configuration. The laser head was placed in front of the endwall of the test section. The laser beam emitted from the laser head goes through the light sheet optics forming the laser sheet, then guided to the test section by two mirrors. The light sheet was inserted into the test section from the endwall window. The position of the laser sheet was preliminary aligned before the camera setup, and its final position and alignment was done with the image calibration plate placed on the measurement plane.

Figure 2-19 shows close-up views of the measurement region in the cascade. A matte-black paint was applied to the central 8 blades and the endwall surface except for the area of the endwall pressure taps. Originally, the laser sheet was planned to be aligned to Plane 06, 0.5Cax downstream of the cascade trailing edge, where the endwall pressure taps and the aerodynamics probe measurements were taken during the main SPLEEN test campaign. However, the PIV measurement on the exact location of Plane 06 was prevented by a significant light reflection on the unpainted endwall surface. Instead, the COP for PIV was axially shifted by 2 mm from Plane 06 ($0.04C_{ax}$) closer to the cascade. At the end of the PIV tests and acquisitions of more than 10000 PIV recordings, the black painted endwall was burnt by the impinging laser sheet. The burned paint absorbs less light, resulting in light reflection of stronger intensity. The increased reflection intensity deteriorated the signal to noise ratio of the PIV images recorded in the last phase of the testing campaign.

Camera 1 and camera 2 were placed in front of sidewall windows 1 and 2, respectively. Camera 1 was equipped with a *Tamron SP AF180 mm f/3.5 Di LD(iF) Macro* lens and camera 2 was equipped with a *AF Micro NIKKOR 200mm f/4 AF-D* lens. Lenses with different focal lengths were used for the two cameras to obtain similar FOVs at different working distances. Each camera was mounted on a Scheimpflug adapter to set the appropriate tilt angle between the camera body and the lens. The optical setup resulted in a scaling factor of about 48 pixels/mm. The cameras were held by a tripod (camera 1) or a traverse system (camera 2) by means of a structure attached to the wind tunnel.

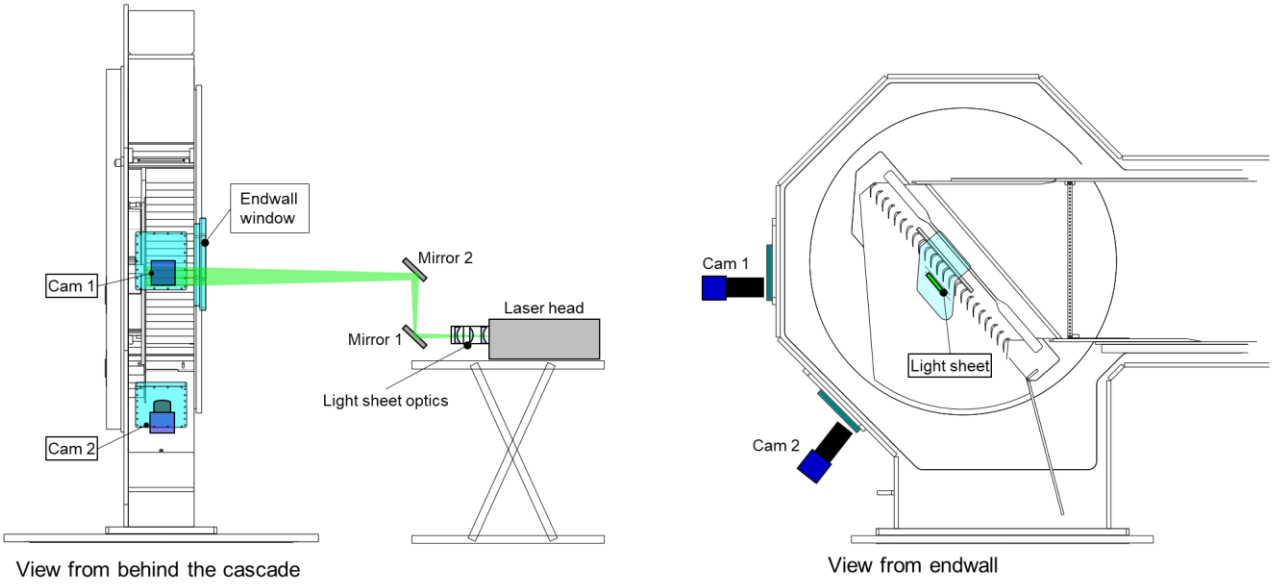

Figure 2-17 Schematics of the laser and camera setup for COP configuration.

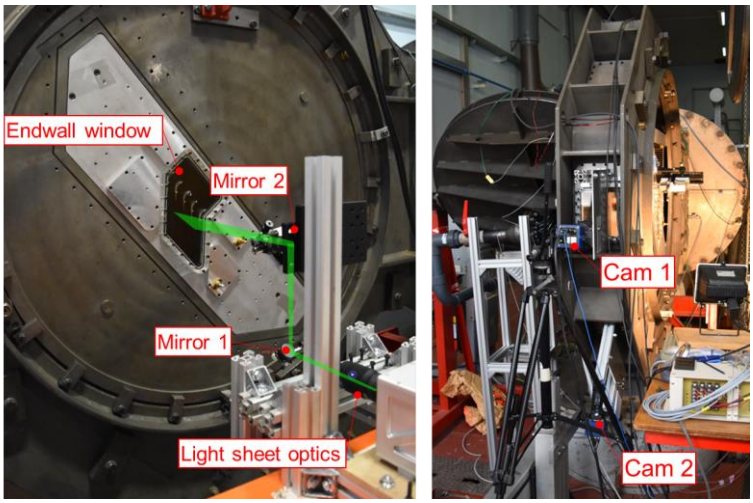

Figure 2-18 PIV setup for COP Passage configuration.

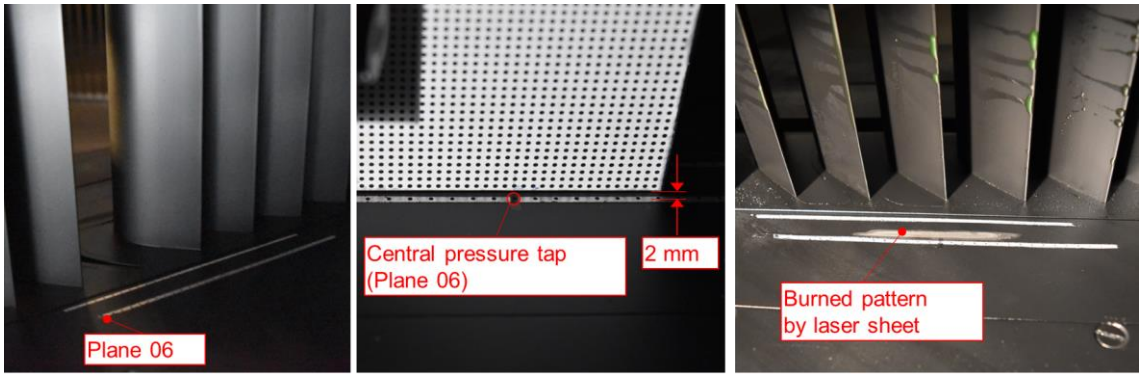

Figure 2-19 Zoomed view of COP measurement location.

2.2.2.1 *Seeding*

Laskin-nozzle seeding generators *PIVTEC PIV Part 14* and *PIV Part 45* were used to produce Di-Ethyl-Hexyl-Sebacat (DEHS) droplets of approximately 1 μm diameter. The particles were seeded downstream of the wind tunnel compressor (upstream of the rig heat exchanger) and in the rig squared upstream of the test section diffuser as indicated in Figure 2-20. The flow seeding located far upstream of the cascade ensured enough distance (over 5 m) to achieve uniform seeding distribution at the test section. The air inlet of the seeding generator was fully opened to atmosphere during the measurement. As the pressure inside wind tunnel was reduced to around 10000 Pa during the test, the air was naturally aspirated into the seeding generator and seeding particles were generated.

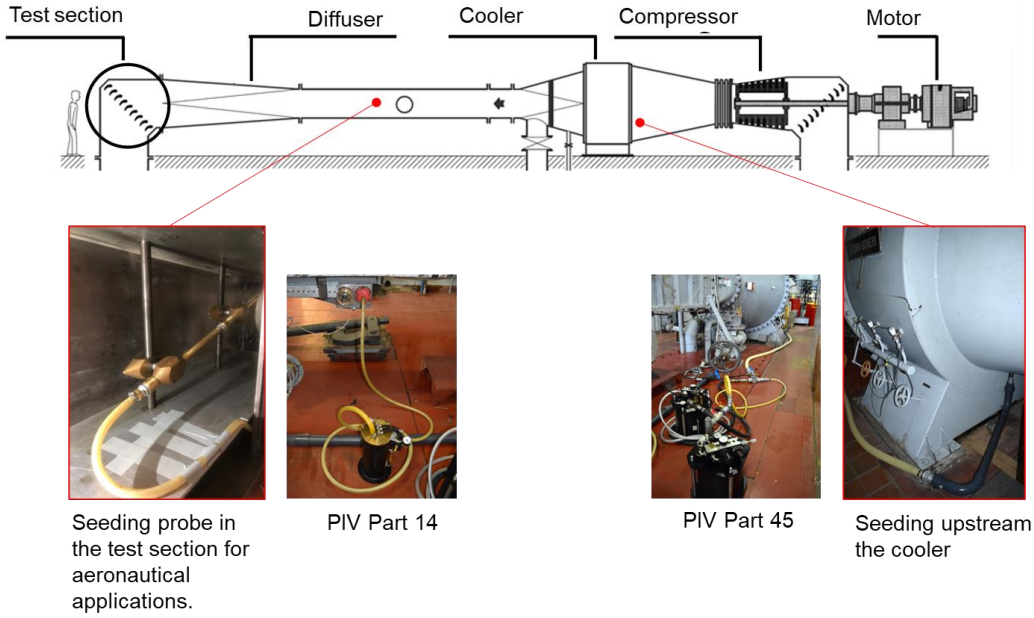

Figure 2-20 Seeding setup for PIV in S-1/C.

2.2.2.2 *Image calibration*

The image calibration was performed using the calibration target images recorded prior to measurements. A single-level calibration target consisting of a regular dot pattern with 1 mm diameter and 2 mm space interval was used for the recording of the calibration images. The target pattern was laser printed on a paper sheet, then it was attached to a 3D-printed base block that fits the cascade shape. The design of the calibration plate is illustrated in Figure 2-21.

The calibration plate was placed in position and traversed using a traverse system as illustrated in Figure 2-22. The traverse system consists of four single-axis stages to realize multi-axis traverse capability. The calibration target plates were held via optical posts and post clamps which allows the user to flexibly tune the target position by sliding and rotating the post.

The system was designed to support all calibration target plates. The following procedure was taken to record calibration images.

1. Place the calibration target in the correct position. (at the blade mid-span for B2B Upstream and B2B Passage, and at the cascade endwall 0.46 x/C_{ax} downstream from the blade TE.)
2. Close the test section except pockets used for calibration plate insertion.
3. Set the camera in place.
4. Record calibration images.
5. For B2B upstream and COP measurements, traverse the plane in plane-normal direction and repeat calibration image recording.
6. Remove the calibration target from the test section through the pocket.
7. Close the pockets used for the calibration plate insertion.
8. Start wind tunnel.

For B2B upstream and COP configuration, multiple calibration images at different normal-to-plane positions were acquired for stereoscopic reconstruction. The target plate was translated in the plane-normal direction, typically at three or five equidistant positions spaced 0.5 or 1.0 mm apart, using one of the traverse stage of the system.

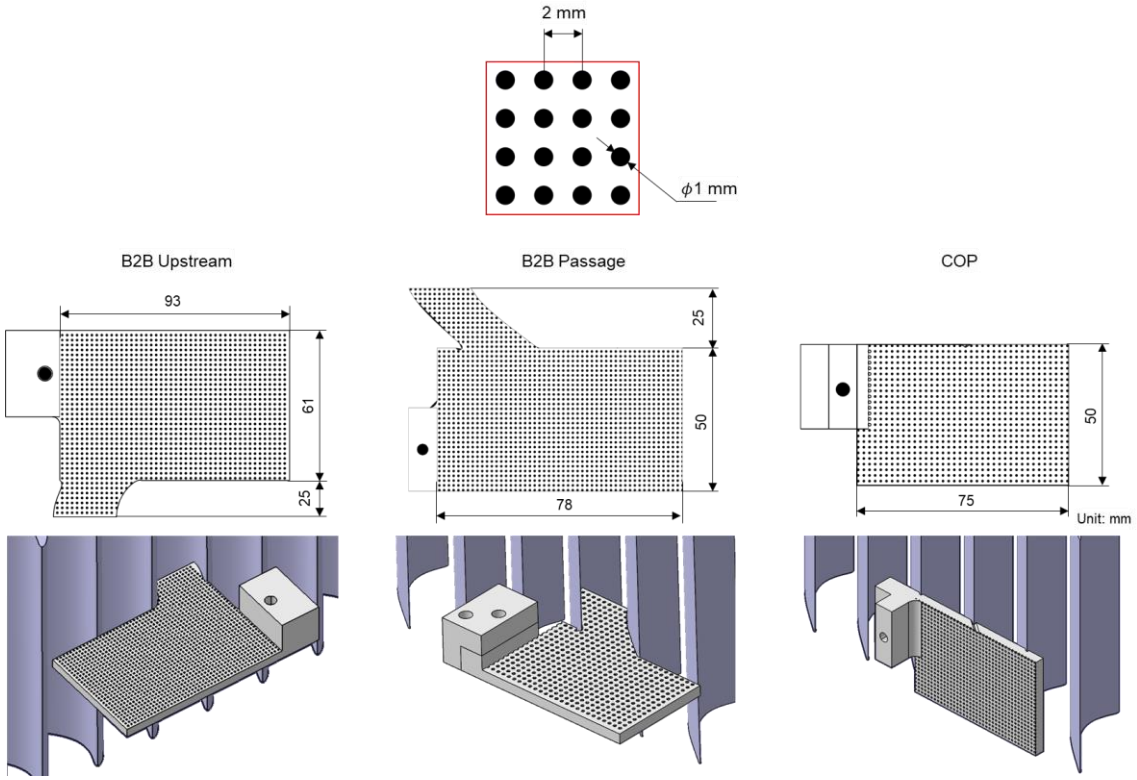

Figure 2-21 Design of calibration plate.

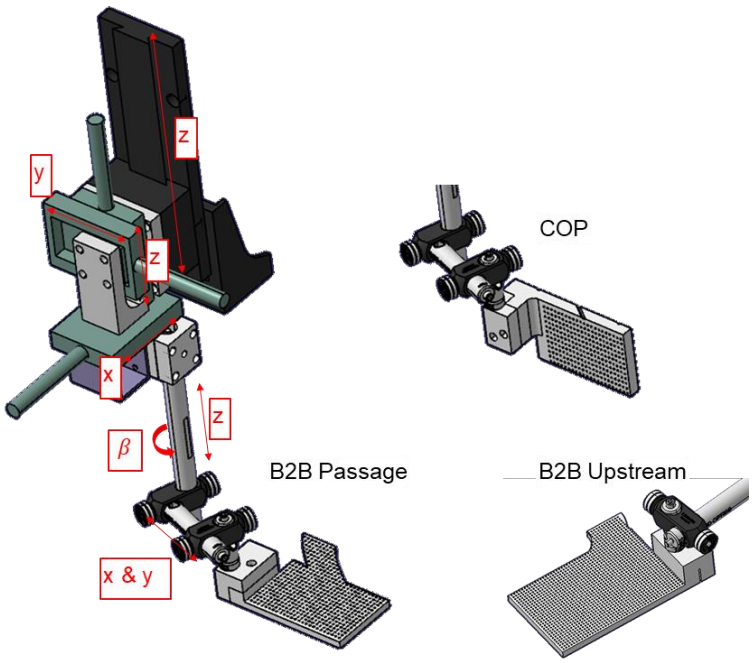

Figure 2-22 Calibration plate traversing system.

The image calibration was performed using the *Davis* PIV processing software. A 3rd order polynomial function was selected as the fitting function to consider arbitrary distortions caused by the optical windows. After image calibration in *Davis*, a conversion of the calibration target coordinate system to the measurement coordinate system was implemented in *MATLAB*.

Figure 2-23 shows the schematics of the B2B upstream coordinate system. The capital and italic symbols indicate measurement and calibration system coordinates, respectively. The leading edge of central blade is set to the origin of the measurement coordinate system O_{meas}. The origin of calibration coordinate system O_{Calib} is aligned to O_{meas} in pitchwise direction while 1.00 mm offset is present in axial direction.

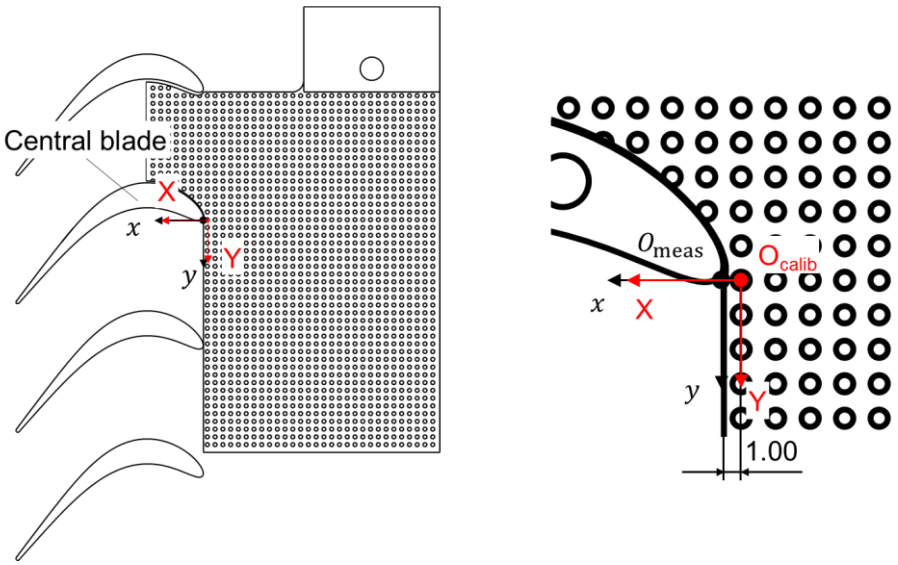

Figure 2-23 Calibration and measurement coordinate systems for B2B upstream configuration.

Figure 2-24 illustrates the schematics of the B2B passage coordinate system. As is the case of B2B upstream, the leading edge of central blade is set to the origin of the measurement coordinate system. The origin of calibration coordinate system O_{Calib} is the first dot downstream of the trailing edge of the central blade. The location of O_{Calib} is aligned to the outlet blade metal angle βmetal, out with 1.50 mm axial offset.

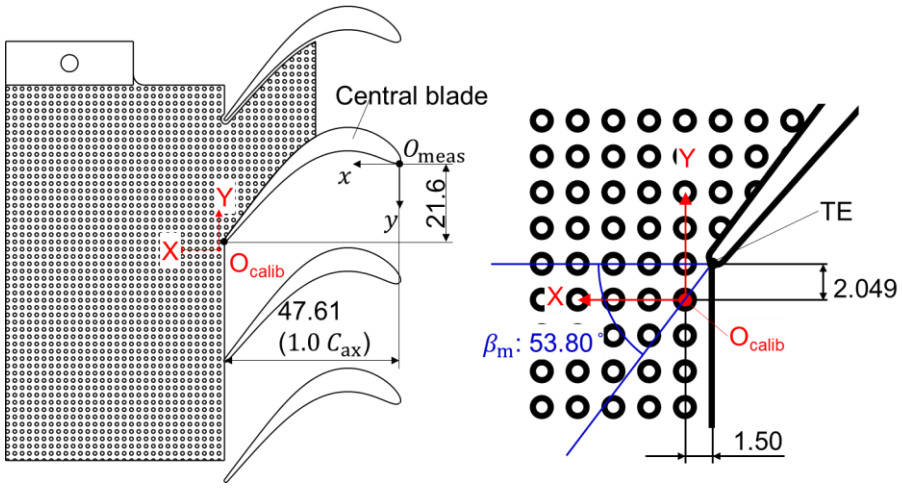

Figure 2-24 Calibration and measurement coordinate systems for B2B passage configuration.

Figure 2-25 shows the schematics of the COP coordinate system. The origin of the local coordinate system for COP (O_{P06}) is the intersection of the outlet metal angle line and Plane 06 (1.5 C_{ax}) located on the endwall (z = 0). However, the PIV plane is traversed 2 mm in upwind axial direction to avoid strong light reflection, thus the origin of calibration coordinate system O_{Calib} is off from both P06 and outlet metal angle line. The origin of local coordinate system for PIV plane O_{P06}, PIV is therefore considered to be the intersection of the outlet metal angle line and the PIV plane (1.46 C_{ax}).

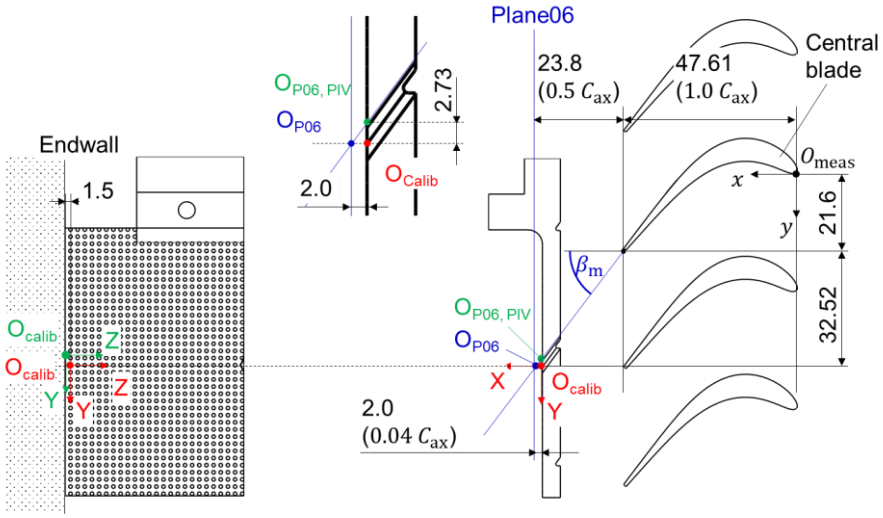

Figure 2-25 Calibration and measurement coordinate systems for COP configuration.

Despite careful positioning of the calibration plates, a small misalignment of the optical system may still be present which can affect the coordinate system. A correction of in-plane misalignment was applied to the coordinate system during a conversion of the calibration target coordinate system to the measurement coordinate system.

2.2.2.3 Image preprocessing

Prior to the vector field computation, image preprocessing was performed to minimize image background noise and strong reflections from the surface hit the by laser sheet. The raw images of the B2B Upstream case underwent subtraction of the temporal-mean image and subtraction of the spatial sliding average with a window size of 11 pixel. For the B2B Passage and COP cases, the subtraction of the temporal-mean image was done on a variable window size ranging between 11 and 51 images, and particle intensity normalization was applied. A case-dependent filter size was utilized to match the image-to-image variation of the noise pattern.

2.2.2.4 Vector computation

The vector fields were computed using *Davis 11* multi-pass cross-correlation algorithm.
For the B2B Upstream case, the size of the starting and final interrogation windows was set to 128 × 128 pixels and 64 × 64 pixels with 50% overlap.
For B2B Passage and COP cases, the size of the starting and final interrogation windows was set to 128 × 128 pixels and 32 × 32 pixels with 50% overlap.
These cross-correlation settings resulted in vector spatial resolutions of 0.73 mm for the B2B Upstream measurement, 0.35 mm for the B2B Passage measurement, and 0.25 mm for the COP measurements. A spatial median filter was applied for outlier removal.

3 Data processing

This section provides the definition of derived quantities that describe the cascade flow (angle, Mach number) and turbulence parameters in addition to data reduction tools and methods employed for the data post-test treatment.

3.1 PIV data processing

The coordinate system used for the POV data is illustrated in Figure 3-1.
The quantities describing the inlet and outlet flow angle are the primary flow direction, β, and the cascade pitch angle, γ. Figure 3-1 displays the positive orientation of the primary flow direction and the cascade pitch angle in the cascade reference system. The primary flow direction can be seen as a projection of the inlet or outlet flow angles on the XY plane. On the other hand, the cascade pitch angle is the projection of the inlet or outlet flow angle on the XZ plane. The values in the database are time-averaged.

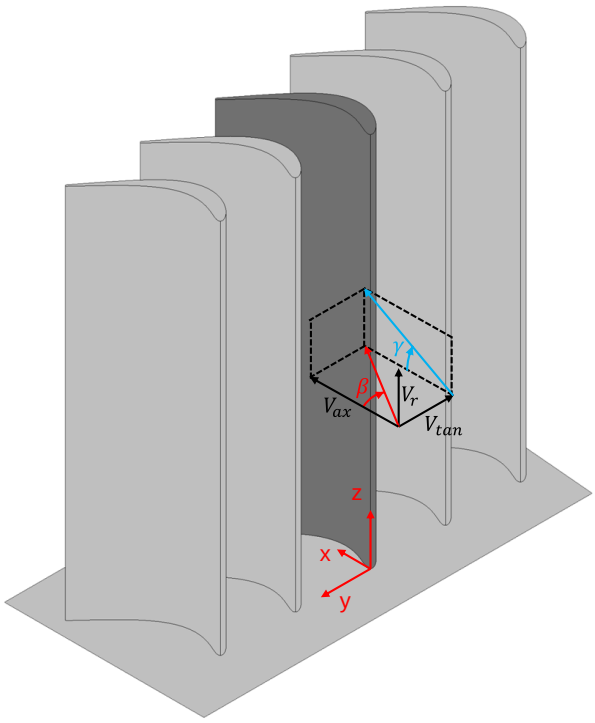

Figure 3-1 Primary flow direction and cascade pitch angle in the cascade reference system.

3.1.1.1 *Velocity components and flow angle*

In PIV measurements, the components of the flow velocity vector are computed from the estimated displacement of particles X_{d_i} in the corresponding direction i, the separation time between two successive laser pulses t_s, and the scaling factor F_s that converts the displacement information from pixel to a physical distance.

$$V_i = F_s \frac{X_{d_i}}{t_s}$$
$$(i = x, y, z, \text{or axi}, \tan, \text{rad})$$

The flow angle is decomposed into two components, the yaw angle (primary flow direction) β and pitch angle γ. The yaw angle is the angle between axial direction and the flow velocity projected on the xy- (axial-tangential) plane. The pitch angle is the angle between the axial direction and the flow velocity projected on the xz- (axial-span) plane. The two components are calculated by:

$$\beta = \tan^{-1}\frac{V_y}{V_x} \text{ or } = \tan^{-1}\frac{V_{\tan}}{V_{\text{axi}}}$$

$$\gamma = \tan^{-1}\frac{V_z}{V_x} \text{ or } = \tan^{-1}\frac{V_{\text{rad}}}{V_{\text{axi}}}$$

For the analysis of secondary flows at the cascade outlet plane, the velocity is decomposed into streamwise, crosswise, and spanwise components (denoted as V_{str}, V_{crs}, and V_{rad}, respectively) using the following equations:

$$V_{\text{str}} = V_{\text{axi}} \cos\beta_{MS} + V_{\tan} \sin\beta_{MS}$$

$$V_{\text{crs}} = V_{\text{axi}} \cos\beta_{MS} + V_{\tan} \sin\beta_{MS}$$

where β_{MS} is the pitch-wise area averaged yaw angle (primary flow angle) at the blade midspan measured by the B2B passage PIV measurements ($\beta_{MS} = \tan^{-1} V_{\tan,MS} / V_{\text{axi},MS}$).

3.1.1.2 *Isentropic Mach number*

The Mach number is the ratio of the speed of the flow $|V|$ to the speed of sound a.

$$M = |V|/a$$

The speed of flow is available from PIV measurements. The speed of sound is defined as:

$$a = \sqrt{\gamma RT}$$

where γ is the specific heat ratio, R is the gas constant, and T is the static temperature. From the isentropic flow equations and the assumption of a perfect gas, the local Mach number can be calculated from the velocity field and the cascade inlet total temperature:

$$M = \sqrt{\frac{V^2}{\gamma RT_0 - \frac{\gamma - 1}{2}V^2}}$$

3.1.1.3 *Turbulence quantities*

The instantaneous velocity components V_i decomposed into the mean quantity $\overline{V_i}$ and the unsteady (turbulence) part V_i'.

$$V_i = \overline{V_i} + V_i'$$

The mean velocity component V_i from the finite number of samples N is computed as:

$$\overline{V_i} = \frac{\sum_{m=1}^{N} V_{i,m}}{N}$$

$V_{i,m}$ is the instantaneous velocity component. The root-mean-square (RMS) of the fluctuating part of each velocity component $V_{i,\mathrm{RMS}}'$ is synonymous with its standard deviation σ_{V_i} calculated as:

$$V_{i,\mathrm{RMS}}' = \sigma_{V_i} = \sqrt{\frac{\sum_{m=1}^{N}\left(V_{i,m} - \overline{V_i}\right)^2}{N-1}}$$

Turbulence intensity

The single component turbulence intensity TI_i is given by:

$$TI_i = \frac{V_{i,\mathrm{RMS}}'}{\overline{|V|}}$$

The two-component turbulence intensity TI_{2D} for i and j components is calculated as:

$$TI_{2D} = \sqrt{\frac{V_{i,\mathrm{RMS}}' + V_{j,\mathrm{RMS}}'}{2}} \Big/ \overline{|V|}$$

The three-component turbulence intensity TI_{3D} for i, j and k components is calculated as:

$$TI_{3D} = \sqrt{\frac{V_{i,\mathrm{RMS}}' + V_{j,\mathrm{RMS}}' + V_{k,\mathrm{RMS}}'}{3}} \Big/ \overline{|V|}$$

3.1.1.4 *Masking function*

In addition to outlier filtering, an additional masking filter was introduced in the data processing using *MATLAB*. The masking filter was created based on allowable vector ranges in terms of the velocity magnitude, the flow direction, and the level of standard deviation. Furthermore, the local uncertainty on particle displacement deduced from correlation statistics[1] was used to remove unreliable vectors. While it was mentioned that the correlation-statistics-based uncertainty cannot detect the spurious vector, the excessive level of uncertainty is attributable to poor image quality and thus the resulting velocity vectors can be tagged

[1] *Wieneke, B. (2015). PIV uncertainty quantification from correlation statistics. Measurement Science and Technology, 26(7), 074002.*

as unreliable. The vectors that have correlation-statistics-based uncertainty larger than 10% of the reference velocity speed (the isentropic outlet flow speed) have been discarded.

4 Uncertainty

4.1 Definitions and error propagation

The measurement uncertainty is evaluated by the ASME Measurement Uncertainty method[2].

The errors have been categorized as "random" for errors that varied during the measurement period and as "systematic" for errors that were invariant during the measurement period.

The combined total uncertainty of a measured quantity can be estimated as:

$$\delta\Phi = \sqrt{\Phi_{sys}^2 + \Phi_{rand}^2}$$

Then, for a generic quantity q depending on independent parameters $\Phi_1, \Phi_2, \Phi_3, \dots, \Phi_n$:

$$q = f(\Phi_1, \Phi_2, \Phi_3, \dots, \Phi_n)$$

The uncertainty propagation into the derived quantity q of all the uncertainty terms is determined through a Taylor Series Method (TSM) with higher-order terms neglected.
For small variations of the parameter Φ_i, the effect of the associated uncertainty $\delta\Phi_i$ on the propagated uncertainty δq can be expressed in linear form:

$$\delta q = \sqrt{\sum_{i=1}^{n} \left(\frac{\partial \mathrm{q}}{\partial \Phi_i}\delta\Phi_i\right)^2}$$

Where the term $\partial q / \partial \Phi_i$ is the sensitivity coefficient expressing the dependence of q on Φ_i.

4.2 Measurement uncertainties

The systematic, random, and overall uncertainties are reported in Table 4-1 for the velocity components measured by PIV. The uncertainty is given for the design flow condition ($Re_{out,is} = 70\text{K}$, $M_{out,is} = 0.90$, with TG). The overall uncertainty is expressed with 95% confidence interval. The uncertainties reported in the table show that systematic terms are generally the largest contributors to the overall measurement uncertainty. The sources of systematic terms are the estimated misalignment of the calibration plates, accuracy of the calibration dot pattern, uncertainty calculated using correlation statistics method[3], and accuracy of the laser pulse timing.
Due to a reduction in seeding quality in the wake region, a dedicated uncertainty for these regions is reported for measurements in the B2B passage and COP planes. The overall PIV uncertainty in the wake regions is higher than in the cascade free-stream regions where seeding was generally stronger.

[2] *R. B. Abernethy, R. P. Benedict, and R. B. Dowdell. ASME Measurement Uncertainty. Journal of Fluids Engineering, 107(2):161, 1985.*
[3] *Wieneke, B. (2015). PIV uncertainty quantification from correlation statistics. Measurement Science and Technology, 26(7), 074002.*

Table 4-1: Measurement uncertainty

			Uncertainty in freestream			Uncertainty in wake		
Quantity	**Symbol**	**Unit**	**Random**	**Systematic**	**Total (95% CI)**	**Random**	**Systematic**	**Total (95% CI)**
Midspan B2B Upstream PIV measurements								
Axial velocity	Vaxi	m/s	0.07	1.84	3.61	NA	NA	NA
Tangential velocity (pitchwise)	Vtan	m/s	0.07	1.84	3.62	NA	NA	NA
Radial velocity (spanwise)	Vrad	m/s	0.14	5.88	11.53	NA	NA	NA
Velocity magnitude (2D, in-plane)	Vmag 2D	m/s	0.07	1.84	3.61	NA	NA	NA
Velocity magnitude (3D)	Vmag 3D	m/s	0.07	1.89	3.70	NA	NA	NA
Yaw angle	Beta	deg	0.03	0.64	1.26	NA	NA	NA
Pitch angle	Gamma	deg	0.06	2.53	4.95	NA	NA	NA
Turbulence intensity (2D, in-plane)	TI 2D	%	NA	NA	0.04	NA	NA	NA
Turbulence intensity (3D)	TI 3D	%	NA	NA	0.06	NA	NA	NA
Midspan B2B Passage PIV measurements								
Axial velocity	Vaxi	m/s	0.07	3.74	7.34	0.69	4.20	8.35
Tangential velocity (pitchwise)	Vtan	m/s	0.07	4.74	9.30	0.45	4.57	9.00
Velocity magnitude (2D, in-plane)	Vmag 2D	m/s	0.07	4.41	8.64	0.56	4.42	8.74
Yaw angle	Beta	deg	0.01	0.79	1.54	0.13	0.93	1.84
Turbulence intensity (2D, in-plane)	TI 2D	%	NA	NA	0.04	NA	NA	0.27
PL06 Cascade outlet plane PIV measurements								
Axial velocity	Vaxi	m/s	0.18	4.92	9.65	0.70	8.40	16.52
Tangential velocity (pitchwise)	Vtan	m/s	0.12	2.95	5.77	0.45	4.00	7.88
Radial velocity (spanwise)	Vrad	m/s	0.17	2.94	5.78	0.45	4.00	7.88
Velocity magnitude (3D)	Vmag 3D	m/s	0.15	3.88	7.61	0.55	5.91	11.64
Yaw angle	Beta	deg	0.03	0.81	1.59	0.15	1.66	3.26
Pitch angle	Gamma	deg	0.05	0.88	1.73	0.18	1.62	3.19
Turbulence intensity (3D)	TI 3D	%	NA	NA	0.06	NA	NA	0.47

List of related publications (up to October 26th, 2023):

L. Simonassi, G. Lopes, S. Gendebien, A. F. M. Torre, M. Patinios, S. Lavagnoli, N. Zeller, L. Pintat, "An Experimental Test Case for Transonic Low-Pressure Turbines - Part 1: Rig Design, Instrumentation and Experimental Methodology," In ASME Turbo Expo 2022: Turbine Technical Conference and Exposition. The American Society of Mechanical Engineers (ASME). GT2022-81566, V10BT30A012; 14 pages https://doi.org/10.1115/GT2022-81566

G. Lopes, L. Simonassi, A. F. M. Torre, M. Patinios, and S. Lavagnoli, "An Experimental Test Case for Transonic Low-Pressure Turbines - Part 2: Cascade Aerodynamics at On- and Off- Design Reynolds and Mach Numbers," In ASME Turbo Expo 2022: Turbine Technical Conference and Exposition (pp. GT2022-82626). The American Society of Mechanical Engineers (ASME). GT2022-82626; V10BT30A027 https://doi.org/10.1115/GT2022-82626

A. F. M. Torre, M. Patinios, G. Lopes, L. Simonassi, and S. Lavagnoli, "Vane-Probe Interactions in Transonic Flows," J. Turbomach. June 2023, 145(6): 061010, https://doi.org/10.1115/1.4056578

Lopes, G., Simonassi, L., Torre, A. F. M., & Lavagnoli, S. (2023, May). Instrumentation Interference in a Transonic Linear Cascade. In Journal of Physics: Conference Series (Vol. 2511, No. 1, p. 012018). IOP Publishing. https://doi.org/10.1088/1742-6596/2511/1/012018

Simonassi L, Lopes G, Lavagnoli S. Effects of Periodic Incoming Wakes on the Aerodynamics of a High-Speed Low-Pressure Turbine Cascade. International Journal of Turbomachinery, Propulsion and Power. 2023; 8(3):35. https://doi.org/10.3390/ijtpp8030035

Lopes G, Simonassi L, Lavagnoli S. Impact of Unsteady Wakes on the Secondary Flows of a High-Speed Low-Pressure Turbine Cascade. International Journal of Turbomachinery, Propulsion and Power. 2023; 8(4):36. https://doi.org/10.3390/ijtpp8040036

Okada, M., Simonassi, L., Lopes, G., and Lavagnoli, S. (October 5, 2023). "PIV MEASUREMENTS IN A HIGH-SPEED LOW-REYNOLDS LOW-PRESSURE TURBINE CASCADE." ASME. J. Turbomach. doi: https://doi.org/10.1115/1.4063674

Lopes, G., Simonassi, L., and Lavagnoli, S. (October 20, 2023). "Aerodynamics of a High-Speed Low-Pressure Turbine Cascade With Cavity Purge and Unsteady Wakes." ASME. J. Turbomach. doi: https://doi.org/10.1115/1.4063878